mGRASP enables mapping mammalian synaptic connectivity with light microscopy

Jinhyun Kim[1,2,5], Ting Zhao[1,3,5], Ronald S Petralia[4], Yang Yu[1], Hanchuan Peng[1], Eugene Myers[1] & Jeffrey C Magee[1]

The GFP reconstitution across synaptic partners (GRASP) technique, based on functional complementation between two nonfluorescent GFP fragments, can be used to detect the location of synapses quickly, accurately and with high spatial resolution. The method has been previously applied in the nematode and the fruit fly but requires substantial modification for use in the mammalian brain. We developed mammalian GRASP (mGRASP) by optimizing transmembrane split-GFP carriers for mammalian synapses. Using *in silico* protein design, we engineered chimeric synaptic mGRASP fragments that were efficiently delivered to synaptic locations and reconstituted GFP fluorescence *in vivo*. Furthermore, by integrating molecular and cellular approaches with a computational strategy for the three-dimensional reconstruction of neurons, we applied mGRASP to both long-range circuits and local microcircuits in the mouse hippocampus and thalamocortical regions, analyzing synaptic distribution in single neurons and in dendritic compartments.

Over the past century, the desire to link neuronal network activity and behavior has driven neuroscientists to develop techniques for mapping synaptic connectivity in neuronal circuits[1–3]. The extent of overlap between the axonal arbor of a presynaptic neuron and the dendritic arbor of a postsynaptic neuron has been used to infer the presence of synaptic connectivity[4] based on the fact that synapse formation requires a physical contact. However, this criterion can only provide an estimate for connection probability as it has been shown that less than half of the axons within reach of a given postsynaptic dendrite actually form functional synaptic contacts[5].

The presence and statistical characteristics of actual synaptic connectivity can be determined by neuronal reconstruction from high-resolution electron microscopy data. But even with recent advances in electron microscopy–related methodology, it remains a relatively time-consuming and volume-limited endeavor to reconstruct a substantial region of neuronal tissue[6,7]. Recently, fluorescence-based methods such as array tomography, Brainbow, trans-synaptic tracing and GRASP[8–11] have emerged as alternative approaches for mapping neuronal circuitry, enabled by sophisticated techniques for genetic manipulation of animal models.

GRASP is based on functional complementation between two nonfluorescent split-GFP fragments (called GFP1–10 and GFP11) tethered to the synaptic membranes in two separate neuronal populations[11]. When two neurons, each expressing one of the fragments, are tightly opposed through a synaptic cleft, fluorescent GFP is reconstituted (**Fig. 1a**) and the location of synapses can be visualized. To date, GRASP has been applied to map synaptic connectivity in the nematode and the fruit fly[11,12]. However, before GRASP can be used as a transmembrane proximity detector for synapse visualization in the mammalian brain, several important modifications are required because of variability of synaptic architecture across organisms[13].

Here we describe optimized GRASP for mapping long-range circuits as well as microcircuits in the mammalian brain (mGRASP). Using *in silico* protein design, we engineered chimeric synaptic mGRASP components that would target to pre- and postsynaptic membranes separately and match the ~20-nm-wide synaptic cleft of mammalian synapses. We validated the synaptic distribution of the designed pre- and postsynaptic mGRASP components with electron microscopy, verified that the reconstitution of mGRASP could be detected in well-studied synapses of various brain regions (for example, Schaffer collateral synapses of the hippocampus) and determined that our technique led to no substantial change in synaptogenesis. We also verified that mGRASP can be used to specifically detect actual synapses, not potential synapses, by examining sites where synapses are known to be absent even if fully surrounded by nontargeting axons. In addition, we report analysis strategies and computational programs for the three-dimensional reconstruction of neurons that allowed us to investigate the localization and detailed subcellular distribution of synapses. Our results show that mGRASP is a powerful tool to characterize both neuronal inhibitory and excitatory circuits in the mouse brain.

RESULTS

mGRASP design and gene-delivery strategy

Our design goals were to produce pre- and postsynaptic proteins that would allow split-GFP reconstitution over synaptic clefts in

[1]Janelia Farm Research Campus, Howard Hughes Medical Institute, Ashburn, Virginia, USA. [2]Center for Functional Connectomics, Korea Institute of Science and Technology, Seoul, Korea. [3]Qiushi Academy for Advanced Studies, Zhejiang University, Hangzhou, China. [4]National Institute on Deafness and Other Communication Disorders, National Institutes of Health, Bethesda, Maryland, USA. [5]These authors contributed equally to this work. Correspondence should be addressed to J.K. (kimj@kist.re.kr) and J.C.M. (mageej@janelia.hhmi.org).

RECEIVED 1 JUNE; ACCEPTED 29 SEPTEMBER; PUBLISHED ONLINE 4 DECEMBER 2011; DOI:10.1038/NMETH.1784

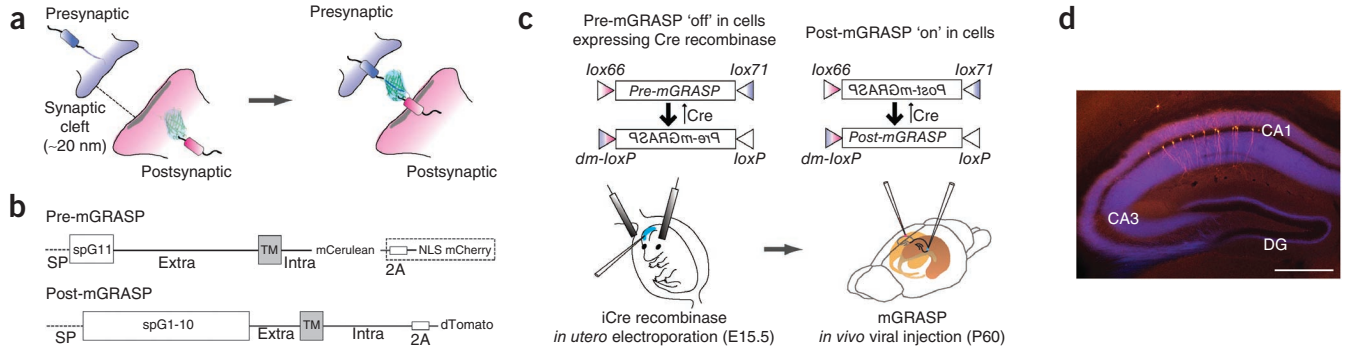

Figure 1 | Synaptic mGRASP components and gene-delivery strategy. (**a**) Schematic illustration of mGRASP in the synapse. (**b**) Diagram of pre- and post-mGRASP composed of signal peptide (SP), split-GFP fragment GFP1-10 (spG1-10) or GFP11 (spG11), extracellular domain (extra), transmembrane domain (TM) and intracellular domain (intra) followed by fluorescent proteins (mCerulean, 2A-mCherry or 2A-dTomato). (**c**) Strategy for cell-type–specific and sparse gene delivery. In addition to Cre recombinase–independent pre- and post-mGRASP, Cre recombinase–dependent 'switch off' pre-mGRASP and 'switch on' post-mGRASP were generated, by using two mutant *loxP* sites (*lox66* and *lox71*) in a head-to-head orientation. Because the double-mutated *loxP* (*dm-loxP*) site shows very low affinity for Cre recombinase and results in no or little inversion (indicated by up arrows), the favorable one-step inversion indicated by down arrows is nearly irreversible, allowing the gene to be stably switched 'on' and 'off' as desired. rAAV vectors for the expression of these constructs were injected into the hippocampus ~2 months after *in utero* electroporation of iCre recombinase on embryonic day 15.5 (E15.5) or into the hippocampus of Cre recombinase–expressing transgenic mice on postnatal day 60 (P60). (**d**) Example dTomato and mCerulean fluorescence merged image shows dense axonal projections of CA3 neurons infected with pre-mGRASP (*aavCAG-pre-mGRASP-mCerulean*; blue) and sparse CA1 pyramidal neurons expressing post-mGRASP (*aavCAG-Jx-rev-post-mGRASP-2A-dTomato*; red). Scale bar, 500 μm.

the mouse brain without causing spurious synapse formation or inappropriate reconstitution at nonsynaptic regions. To do so, we searched for suitable transmembrane molecules that are localized restrictedly at synapses. In the mammalian central nervous system, overexpression of certain synaptic molecules, such as neurexin and neuroligin, can cause changes in synapse morphology leading to increased maturation of excitatory synapses and respective changes in physiology and behavior[14–16]. Thus, we designed *in silico* chimeric pre- and postsynaptic mGRASP components, synthesized from publicly available sequences (US National Center for Biotechnology Information; NCBI) and codon-optimized for *Mus musculus* (Online Methods). We wanted to ensure that mGRASP components were targeted to and maintained at synapses and that the extracellular domains including the split-GFP fragments fit appropriately in the synaptic cleft (**Fig. 1a**).

Both pre- and postsynaptic mGRASP components were composed of an N-terminal signal peptide followed by a split-GFP fragment, an extracellular domain, a transmembrane domain, an intracellular domain and a fluorescent protein for neurite visualization (**Fig. 1b**). For the presynaptic mGRASP component (pre-mGRASP), we used as a signal peptide the first 29 residues of the nematode β-integrin (PAT-3, residues 1–29) followed by the 16-residue GFP11, two Gly-Gly-Gly-Gly-Ser (GGGGS) linkers, and the extracellular domain and predicted transmembrane domain of human CD4-2 (residues 25–242, as in the original GRASP)[11]. To target and maintain this construct specifically in presynaptic sites, we included as an intracellular domain the 55-residue C terminus of the rat neurexin-1β (residues 414–468) containing the PDZ-binding motif necessary for endoplasmic reticulum and Golgi exit and synaptic targeting[14]. Finally, to visualize pre-mGRASP, we fused monomeric (m)Cerulean to the construct. For the postsynaptic mGRASP component (post-mGRASP), we used mouse neuroligin-1 as the main skeleton. Full-length neuroligin-1 contains 575 residues of a catalytically inactive esterase domain (residues 52–626) that are known to interact with presynaptic neurexin, leading to synapse formation[15]. Thus, we deleted residues 52–626 completely to avoid nonspecific synaptogenesis via interactions with endogenous neurexin. We inserted the 648-residue GFP1-10 fragment after the signal peptide (residues 1–49) of the esterase-truncated neuroligin-1. The rest of post-mGRASP consisted of the 71-residue extracellular domain, the 19-residue predicted transmembrane domain and the 127-residue C terminus of mouse neuroligin-1. In addition, we fused dimeric (d)Tomato to the cytosolic end of post-mGRASP via the self-cleavable 2A peptide[17] to visualize the morphology of the postsynaptic cells.

Before deciding on these configurations we attempted other combinations that all led to failures: different signal peptides (for example, of neurexin and the *Drosophila* cuticle protein CP3); different extracellular and transmembrane domains (for example, of neurexin and CD8); and different intracellular domains (for example, of Kv4.2 and the myosin-binding domain of mouse melanophilin). Most of these constructs resulted in cytotoxicity, inadequate synaptic expression and/or no fluorescence reconstitution (**Supplementary Fig. 1**). Notably, the CD4-based GRASP system, previously used in the nematode and the fruit fly[11,12] appeared to be nonspecific for endogenous synapse visualization in mammals. Rat hippocampal neurons separately transfected with vectors containing *CD4-GFP1-10* and *CD4-GFP11* and cultured together, as well as mouse brain tissue transduced with recombinant adeno-associated virus (rAAV) vectors for the expression of CD4–GFP1-10 and CD4-GFP11, showed nonspecific line-like fluorescence patterns in addition to the expected puncta-like fluorescence.

Our next challenge was to deliver the pre- and post-mGRASP components into defined neuronal populations without expressing them together in the same cell. To test our pre- and post-mGRASP constructs in the mouse brain, we focused on the well-studied CA3-CA1 connectivity of the hippocampus. We sought to sparsely label postsynaptic CA1 neurons to enable resolution of individual cells and their dendrites in a way suitable for subsequent automated reconstruction. To achieve cell type–specific and sparse

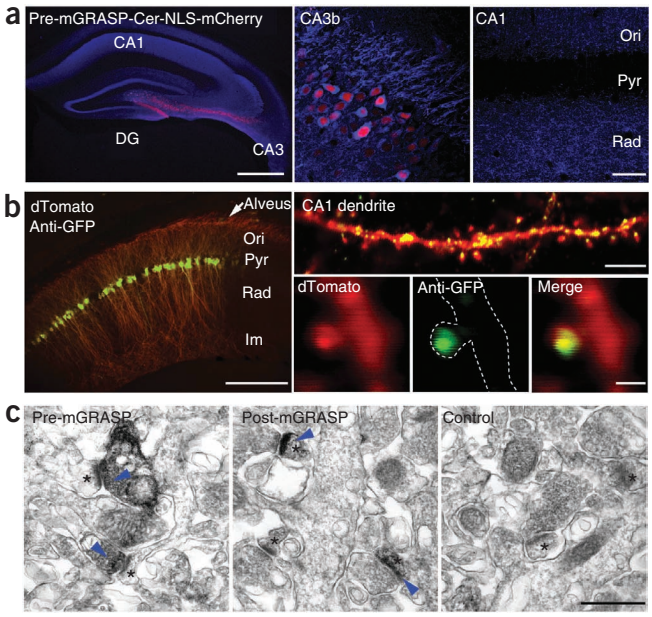

Figure 2 | Synaptic expression of mGRASP components. (**a**) Distribution of Cre recombinase–independent pre-mGRASP (*aavCAG–pre-mGRASP–mCerulean-2A-nls-mCherry*; pre-mGRASP-Cer-NLS-mCherry) visualized with blue fluorescence signals from mCerulean. Overview of the hippocampus (left) and high-magnification images of subregions (CA3b and CA1) show infected cell nuclei in red (mCherry) and their axonal projections in blue (pre-mGRASP–mCerulean). Ori, stratum oriens; pyr, stratum pyramidale; and rad, stratum radiatum. Scale bars, 500 µm (left) and 40 µm (right). (**b**) Dendritic distribution of post-mGRASP (paavCAG-post-mGRASP-2A-dTomato) in CA1 pyramidal neurons visualized by fluorescence immunostaining using polyclonal antibody to GFP (anti-GFP). Cytosolic signal from dTomato is indicated with an arrow (left). High-magnification images show that post-mGRASP appears to be enriched in the postsynaptic density (right). Lm, stratum lacunosum-moleculare. Scale bars, 250 µm (left), 5 µm (right top) and 1 µm (right bottom). (**c**) Immunoelectron microscopy images of pre-mGRASP, post-mGRASP and nontransduced hippocampi as a control using polyclonal anti-GFP. Asterisks indicate postsynaptic density, and blue arrowheads indicate immuno-silver-gold particles. Scale bar, 500 nm.

gene delivery, we used a combination of *in utero* electroporation[18] of Cre recombinase expression plasmids with spatially restricted injection of Cre recombinase–dependent or –independent rAAV vectors for the expression of mGRASP components to ipsilateral and contralateral sides of the hippocampus (**Fig. 1c** and **Supplementary Note 1**). Thus we achieved selective and sparse labeling in ~50–200 postsynaptic CA1 pyramidal neurons without overlap with presynaptic CA3 neurons (**Fig. 1d**).

The combination of gene-delivery strategies allowed us not only to control the sparseness of labeling but also to avoid long-term expression of exogenous synaptic proteins. In addition, the Cre recombinase–dependent viral vectors allow a wide choice of cell type–specific expression of mGRASP components by use of pre-existing and newly generated *Cre* transgenic mouse lines (for example, Gene Expression Nervous System Atlas; GENSAT). To test this, we applied Cre recombinase–dependent 'switch off' pre-mGRASP and 'switch on' post-mGRASP to mouse lines with cell type–specific Cre recombinase expression (**Fig. 1c**). As discussed below, this strategy is especially suitable for labeling of distinct but spatially close cell populations and for mapping local synaptic connectivity.

Synaptic expression of pre- and post-mGRASP

To determine the synaptic expression of pre- and post-mGRASP, we introduced them separately into CA3 and CA1 neurons in the mouse hippocampus and examined their distribution using light and electron microscopy (**Fig. 2**). In the CA3 region, injected with rAAV vector expressing pre-mGRASP fused to mCerulean (*aavCAG–pre-mGRASP–mCerulean*), we detected blue fluorescence only in axonal projections, making it difficult to identify the infected neurons (**Supplementary Fig. 2**). Thus, to facilitate the visualization of infected cells, we generated a new construct including mCerulean-fused pre-mGRASP followed by the self-cleavable 2A peptide and nucleus-targeted nuclear localization sequence (NLS)-mCherry (*aavCAG–pre-mGRASP–mCerulean-2A-NLS-mCherry*). We injected rAAV vectors for the Cre recombinase–independent expression of pre-mGRASP–mCerulean-2A-NLS-mCherry into the CA3 area (**Fig. 1b**). Under light microscopy, we observed strongly labeled blue axons in both ipsilateral and contralateral sides of hippocampi. High-magnification images of infected CA3 areas showed infected cell nuclei labeled with NLS-mCherry and their mCerulean-labeled axonal projections, whereas images of the non-infected CA1 area showed only axonal projections of CA3 neurons (**Fig. 2a**) and confirmed primary axonal expression of pre-mGRASP. In addition, under electron microscopy, silver-gold immunolabeling of mCerulean with an antibody to GFP allowed us to confirm that the pre-mGRASP component was effectively targeted to presynaptic sites (**Fig. 2c**).

To verify correct post-mGRASP expression, we used immunofluorescence staining. As post-mGRASP comprises most of the β-barrel structure of GFP (GFP1-10), many commercially available polyclonal antibodies to GFP can recognize post-mGRASP. We transfected CA1 progenitor cells of the right hemisphere with Cre recombinase–independent post-mGRASP plasmid (paavCAG-post-mGRASP-2A-dTomato) via *in utero* electroporation and visualized its expression pattern 2 months later by immunostaining with an antibody to GFP (**Fig. 2b**). The expression of post-mGRASP appeared to be highly restricted to dendritic branches and was not detectable in axons of CA1 neurons. High-magnification images under light microscopy, as well as immunolabeled images under electron microscopy showed that post-mGRASP was highly enriched in the postsynaptic density (**Fig. 2b**,**c**). Notably, both pre- and post-mGRASP appeared to be expressed throughout even in long neurites as we detected pre-mGRASP along CA3 axonal fibers several millimeters in length and post-mGRASP up to the ends of both apical and basal dendrites of CA1 pyramidal neurons. Taken together, we confirmed that our mGRASP components were targeted into synaptic sites as intended and that mGRASP is appropriate for mapping long-range circuits.

Detection of mGRASP in the mouse brain

We next assayed mGRASP reconstitution in the mouse brain. As we aimed to reconstruct postsynaptic neurons, we labeled postsynaptic CA1 neurons sparsely while densely labeling presynaptic CA3 neurons. We used *in utero* electroporation to provide plasmid encoding improved (i)Cre recombinase[19] (paavCAG-iCre) to the right ventricle of embryos, and, 2 months later, we injected rAAV vectors in the same mice for the expression of

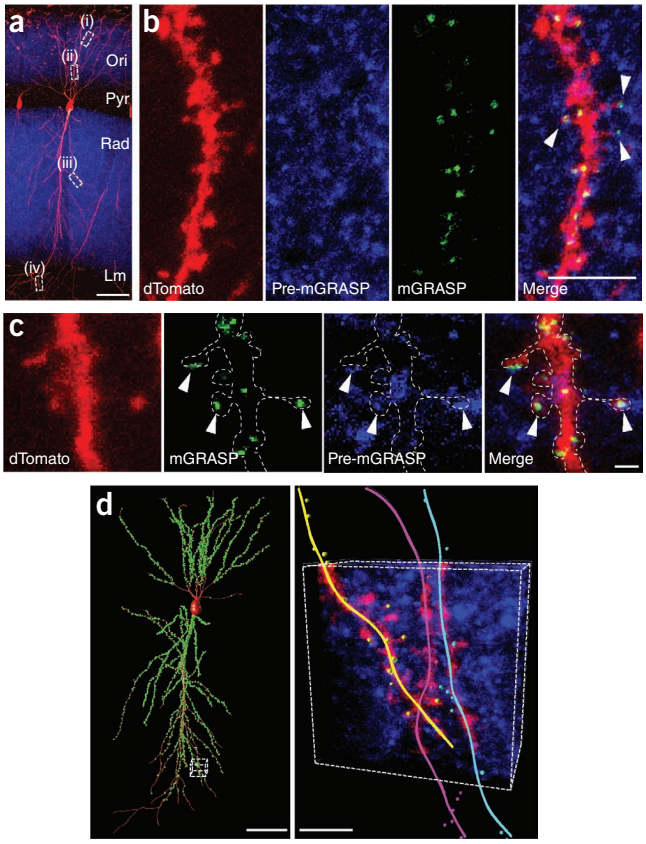

Figure 3 | Reconstitution of mGRASP in hippocampal CA3-CA1 connectivity. (**a**) Discrete puncta of reconstituted mGRASP fluorescence in one CA1 neuron in **Supplementary Figure 3**. Ori, stratum oriens; pyr, stratum pyramidale; rad, stratum radiatum; and lm, stratum lacunosum-moleculare. Scale bar, 100 µm. (**b**,**c**) Cropped high-magnification images of dendrites (dashed boxes (i) in **b**, (ii) in **c** and (iii) and (vi) in **Supplementary Fig. 3**) with reconstituted mGRASP signals in the spine heads in which blue axons intersected with red dendrites (arrowheads). Scale bars, 5 µm (**b**) and 1 µm (**c**). (**d**) An example of reconstructed dTomato-labeled CA1 neurons; locations of synapses were automatically detected in three dimensions following steps 1–3 in **Supplementary Figure 5** (left). Cropped image illustrating synapse detection (colored spheres) in dendritic branches (right). Scale bars, 500 µm (left) and 4 µm (right).

Cre recombinase–independent pre-mGRASP (*aavCAG-pre-mGRASP-mCerulean*) and Cre recombinase–dependent 'switch-on' post-mGRASP (*aavCAG-Jx-rev–post-mGRASP–2A-dTomato*) components into CA3 neurons of the left hemisphere and CA1 neurons of the right hemisphere, respectively. We found that, although neither split-GFP fragment fluoresced when expressed individually, mGRASP was reconstituted trans-synaptically, revealing discrete puncta of fluorescence along dTomato-labeled CA1 apical and basal dendrites in locations where mCerulean-labeled CA3 axons and dTomato-labeled CA1 dendrites intersect (**Fig. 3**, **Supplementary Fig. 3** and **Supplementary Video 1**). Fluorescence signals of reconstituted mGRASP were clearly evident in both the apical and basal dendritic structures of a CA1 neuron, whereas no signals were evident along tuft dendrites in the stratum lacunosum-moleculare where axons from CA3 do not project (**Supplementary Fig. 3b**). High-magnification images showed strong mGRASP signals in the spine heads of both apical and basal dendrites where mCerulean-labeled axons intersected with red dendrites (**Fig. 3c** and **Supplementary Video 2**).

Furthermore, we tested mGRASP reconstitution in another long-range circuit, the thalamocortical circuit, connecting the ventral posterior medial nucleus of the thalamus with layer 4 (L4) neurons of the somatosensory cortex. Using rAAV viral injection, sequences encoding Cre recombinase–independent pre-mGRASP and Cre recombinase–dependent 'switch-on' post-mGRASP were transduced respectively into the thalamic ventral posterior medial nucleus and somatosensory cortex of *Six3-Cre* mice, expressing Cre recombinase mainly in layer-4 neurons[20]. Similar to results obtained with mGRASP in the hippocampus, we detected clear and strong reconstituted mGRASP puncta in sites where dTomato-labeled L4 neurons and mCerulean-labeled thalamic axons intersected (**Supplementary Fig. 4**).

To investigate the localization and distributions of synapses using mGRASP in dendritic compartments and in single cells, we developed analysis strategies and computational programs (**Supplementary Fig. 5** and **Supplementary Note 2**). Using our mGRASP detection program, the number and locations of synapses at the level of dendritic branches were automatically detected in three dimensions (**Fig. 3c**) with ~93.5% accuracy verified by comparison with annotation of randomly selected subvolumes (128 × 128 × 77 voxels) of neuTube-reconstructed neurons by multiple individuals (Online Methods, **Supplementary Note 2** and **Supplementary Software**).

Validation of mGRASP

To test whether mGRASP can be used to detect synapses in the mouse brain without introducing artifacts, we first examined whether mGRASP induces changes in synaptic organization. We analyzed a region of massively reconstituted mGRASP signals with conventional electron microscopy to check the morphology and abundance of excitatory synapses identified by the ultrastructure of postsynaptic densities and presynaptic vesicles. We found no differences in the number of excitatory synapses between hippocampi infected with both pre- and post-mGRASP, non-infected hippocampi and hippocampi infected with only single mGRASP components (**Supplementary Fig. 6**). Notably, our method for gene delivery did not cause any alteration in the number of synapses, compared to nontransduced neurons.

To measure whether mGRASP detects actual synapses rather than neurite touches, we analyzed cell populations known to be synaptically connected as well as ones known to not be synaptically connected (that is, CA1 pyramidal neurons–oriens-lacunosum moleculare (OLM) interneurons as a synaptic pair, and CA3 pyramidal neurons–OLM interneurons as a non-synaptic pair)[21,22]. This test is powerful because axons of both CA3 and CA1 neurons intersect with dendrites of OLM cells, but mGRASP should detect only actual synaptic contacts from CA1 axonal projections and not from CA3 neurons. To express post-mGRASP selectively in OLM cells, we used the Cre recombinase–dependent 'switch-on' post-mGRASP in a genetically manipulated mouse line expressing Cre recombinase under the control of the endogenous somatostatin promoter via knock-in (*sst-Cre*). To label a negative presynaptic partner of the OLM interneurons, we injected rAAV vectors expressing Cre recombinase–independent pre-mGRASP into CA3 neurons. For a positive presynaptic partner of the OLM interneurons, we injected the

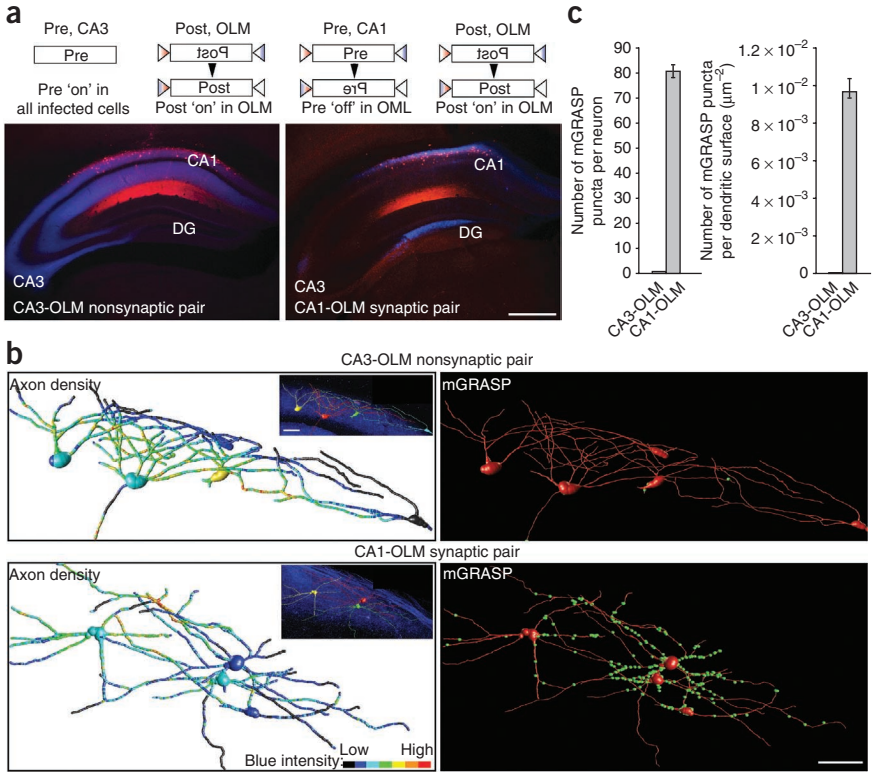

Figure 4 | mGRASP detects actual synapses with high specificity. (**a**) For a nonsynaptic pair (CA3-OLM), unconditional pre-mGRASP and Cre recombinase–dependent 'switch-on' post-mGRASP constructs were injected into CA3 and CA1 of the *sst-Cre* mouse, separately. For a synaptic pair (CA1-OLM), both Cre recombinase–dependent 'switch-off' pre-mGRASP and 'switch-on' post-mGRASP were injected into CA1 of the *sst-Cre* mouse. dTomato and mCerulean fluorescence merged images show blue axonal projections from CA3 and CA1, and post-mGRASP expression in OLM cells. In the merged image of a synaptic pair, blue axons of a small fraction of granule cells were additionally detected but the usual pattern of exclusive CA1 axonal projections is shown in **Supplementary Figure 2**. Scale bar, 500 µm. (**b**) Low to high axon density of CA3 and CA1 surrounding post-mGRASP–expressing OLM cells presented in a color-coded reconstruction; insets indicate locations of OLM cells along with axonal projections (left). mGRASP puncta detected in CA1-OLM as compared to CA3-OLM (right). Scale bars, 50 µm. (**c**) Quantification of mGRASP detections per cell (0.989 ± 0.169 mGRASP puncta, n = 61 cells from 3 mice for CA3-OLM and 80.383 ± 4.992 mGRASP puncta, n = 65 cells from 3 mice for CA1-OLM: mGRASP density per dendritic surface area; 6.05×10^{-5} µm^2 ± 0.82×10^{-5} µm^2, n = 5 stitched image stacks from three mice for CA3-OLM and 9.6×10^{-3} µm^2 ± 1.05×10^{-3} µm^2, n = 5 stitched image stacks from three mice for CA1-OLM). Error bars, s.e.m.

Cre recombinase–dependent 'switch-off' pre-mGRASP into CA1 neurons to avoid expressing both mGRASP components in the same cell, as described above, because they are spatially close to one another (**Figs. 1b** and **4a**). To measure connection probability, we quantified the availability of axons in the local environment surrounding OLM dendrites by measuring the average intensity of blue signal in the same expanded tubes of reconstructed OLM dendrites that we used for mGRASP detection (radius of the traced tube plus ~2.5 µm) (**Fig. 4b**). In the case of the negative synaptic CA3-OLM connections, we detected little or no reconstituted mGRASP puncta, although we saw many axon-dendrite intersections (**Fig. 4b**,**c**). Of the few mGRASP puncta detected in CA3-OLM connections, over 78% occurred on somata and likely reflect innervations from other interneurons in CA1 neurons. By contrast, we observed many reconstituted mGRASP puncta in CA1-OLM connections, especially on dendrites of OLM cells. Overall, we found clear results in mGRASP detection from negative and positive synaptic partners with the same postsynaptic populations: as predicted, we detected mGRASP signals exclusively in CA1-OLM connections and not in CA3-OLM connections. Additionally, using antibodies to GFP shown to have preferred specificity for reconstituted forms of GFP[12], we detected immuno-gold particles by electron microscopy in the synapses (**Supplementary Fig. 7**). Together, these results indicate that with high specificity, mGRASP detected actual synapses rather than neurite touches and induced no obvious artifact effects on synaptic organization. Thus mGRASP expression fulfills our criteria for specific labeling of actual synapses without inducing aberrant synapse formation.

Excitatory and inhibitory synapses with mGRASP

Our automated reconstruction and detection programs can detect synapses and distinguish them from the dendritic compartments of other nearby neurons (**Fig. 5**). We then sought to develop an automated method to distinguish between excitatory and inhibitory synapses based on the size and shape of mGRASP signals. Taking advantage of reports that all synaptic inputs converging onto the perisomatic area of CA1 pyramidal neurons are inhibitory[23], we compared fluorescent mGRASP signals from somata and from dendrites of CA1 neurons. We observed that mGRASP fluorescent puncta on somata were always large and elliptical, whereas those on dendrites were small and round (**Fig. 5**), supporting a classification scheme. In addition, to confirm contralateral inhibitory synapses, as we used contralateral presynaptic projections in this study, we examined contralateral projections of CA3 interneurons using a genetically manipulated mouse line expressing Cre recombinase under the control of the endogenous glutamic acid decarboxylase promoter via knock-in (*GAD-iCre*). We observed contralateral projections of GAD interneurons in both oriens and radiatum of CA1 when we delivered Cre recombinase–dependent rAAV vector for the expression of dTomato specifically into GAD interneurons in CA3 (**Supplementary Fig. 8**). This indicates that large and strong signals from reconstituted mGRASP puncta on the main trunk of the CA1 neuron were likely inhibitory inputs (**Supplementary Fig. 3a**). To investigate the locations and distributions of synapses in depth in dendritic compartments and in single cells, we constructed dendrograms with separate apical and basal dendrites of CA1 and plotted the locations of synapses on them

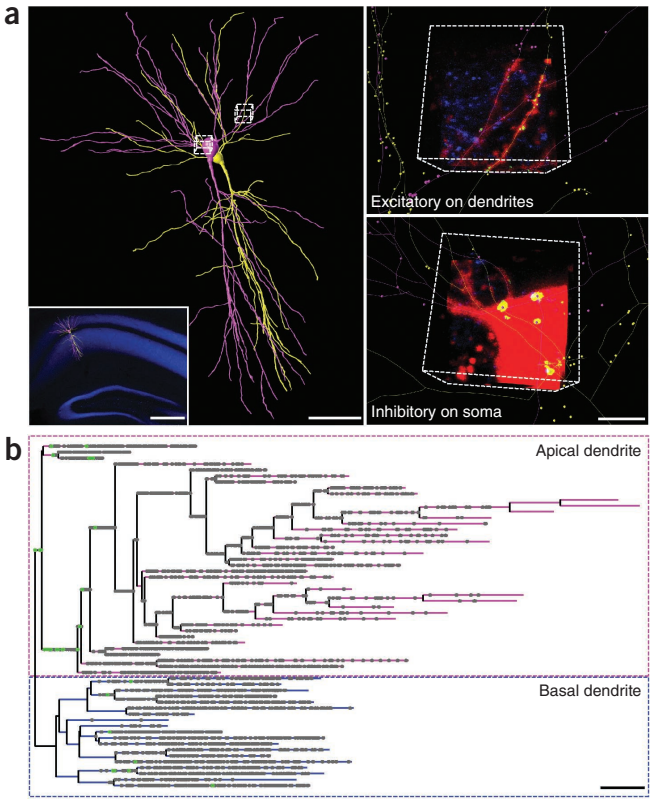

Figure 5 | Distribution of excitatory and inhibitory synapses revealed by mGRASP. (**a**) Representative result of automated reconstruction and mGRASP detection for two nearby neurons (left). Excitatory and inhibitory synapses were automatically distinguished based upon the size and shape of mGRASP signals in somata and dendrites; image details are shown at right. Scale bars, 250 µm (left inset), 50 µm (left) and 4 µm (right). (**b**) Dendrogram illustrating mGRASP detected on a CA1 neuron, showing the lengths of dendrites and locations of synapses in dendritic compartments. Gray dots, excitatory synapse; green dots, inhibitory synapses; magenta, apical dendrites; blue, basal dendrites. Scale bar, 25 µm.

as detected by mGRASP (**Fig. 5b**). Detailed descriptions of the synaptic distributions on dendritic compartments will be critical for a full understanding of their contribution to synaptic signaling and dendritic integration.

DISCUSSION

We presented our initial efforts to determine the location and distribution of synapses in the mouse brain using mGRASP. The method can allow rapid and precise characterization of synaptic connectivity in neuronal circuits in conditions of health as well as in models of neurological disorders that may be caused by abnormal synaptic connectivity, such as autism[24].

In recent years, new optogenetic approaches (for example, based on channelrhodopsin expression) have accelerated the light microscopy–based analysis of synaptic connectivity and synaptic strength[25,26], yet these techniques operate at relatively low levels of resolution and can yield ambiguous results. More recent studies have approached 'functional connectomics' by combining light microscopy–based calcium imaging with electron microscopy–based connectivity mapping in locations such as the mammalian retina and visual cortex[3,27]. However, only relatively small brain volumes, and in particular thin vertical ranges (~50–60 µm), can presently be imaged, mainly because electron microscopy image acquisition and analysis remains a formidable challenge. Alternatively, Brainbow, a light microscopy–based technique integrating genetic manipulation of neurons, can allow synapses to be inferred from neurite contacts by coloring individual neuronal processes differently. This technique, however, appears to be effective for only a subset of synaptic connections[9]. Another light microscopy–compatible method relies on the anterograde and retrograde trans-synaptic tracing of neuronal circuits, but, to date, toxicity issues and biased cell-type specificity of trans-synaptic tracers have limited the utility of the technique[10]. Finally, array tomography, a combination of light microscopy– and electron microscopy–based approaches used to resolve proteomic details at synapses by immunolabeling of multiple synaptic markers, relies entirely on the efficiency of antibody staining and preserved tissue antigenicity, and can result in potentially ambiguous and incomplete results[28]. Our optimized mGRASP system, combined with computer-based three-dimensional (3D) reconstruction of neurons, will complement electron microscopy and optogenetic efforts toward an integrated 3D brain atlas, and can greatly accelerate comprehensive studies of synaptic long-range circuits and microcircuits.

By rapidly revealing the patterns of synaptic connectivity, this approach will enable future studies, but additional challenges and promises remain. To investigate synaptic connectivity in different brain areas, the mGRASP system may need specialized optimizations for different types of synapses. As outlined here, these optimizations could include tailored computational analysis routines and additional versions of mGRASP components with different transmembrane carriers to provide a range of proximities between synaptic membranes. When possible, care should be taken to apply the appropriate validation methods described above to any additional brain regions under study. Furthermore, it will be essential to expand the genetic toolbox for targeting dense or sparse gene expression in desired cell types in different brain areas. Additional promoters for individual cell types, new combinations of multiple genetic switches, different viral systems and creative combinations of all the above with well-characterized transgenic lines (for example, GENSAT) will expand the range of possible experiments. Also, split fluorescent proteins of different colors or photoactivable versions of these proteins will allow the reconstruction of multiply innervated networks with overlapping connectivity patterns. In addition, activity-dependent mGRASP systems can allow the determination of how certain circuits relate to specific behavioral tasks. Thus, additional purpose-driven optimization of mGRASP can provide information about synaptic variation, development and abnormality in intricate networks.

METHODS

Methods and any associated references are available in the online version of the paper at http://www.nature.com/naturemethods/.

Accession codes. GenBank: JN898959 (Cre-dependent rAAV vector), JN898962 (Cre-independent rAAV vector), JN898960 (post-mGRASP component fused to 2A-dTomato) and JN898961 (pre-mGRASP component fused with mCerulean).

Note: Supplementary information is available on the Nature Methods website.

ACKNOWLEDGMENTS

We thank A. Losonczy for valuable discussions and preliminary physiological experiments, R. Sprengel for valuable discussions and help with the 2A-peptide, C. Bargmann (Rockefeller University) the ace-4-CD4spGFP1-10 and rig-3p-CD4spGFP11 expression constructs[11], K. Swartz for simulation of molecular length, B.V. Zemelman (University of Texas at Austin) for the *sst-Cre* and *GAD-Cre* mouse lines and Y.-X. Wang for help with the immuno-silver-gold study. This work was supported by Howard Hughes Medical Institute, US National Institute on Deafness and other Communication Disorders intramural research program, as well as the World Class Institute Program of the National Research Foundation of Korea funded by the Ministry of Education, Science and Technology of Korea.

AUTHOR CONTRIBUTIONS

J.K. designed mGRASP components and performed molecular biology, animal surgery, imaging and data analysis. T.Z. and E.M. developed the image stitching and neuron tracing programs. Y.Y. and H.P. developed the mGRASP puncta detecting program. R.S.P. performed electron microscopy experiments. J.K. and J.C.M. wrote the manuscript.

COMPETING FINANCIAL INTERESTS

The authors declare no competing financial interests.

Published online at http://www.nature.com/naturemethods/.
Reprints and permissions information is available online at http://www.nature.com/reprints/index.html.

1. Neher, E. & Sakmann, B. Single-channel currents recorded from membrane of denervated frog muscle fibres. *Nature* **260**, 799–802 (1976).
2. Buzsaki, G. Large-scale recording of neuronal ensembles. *Nat. Neurosci.* **7**, 446–451 (2004).
3. Bock, D.D. *et al.* Network anatomy and *in vivo* physiology of visual cortical neurons. *Nature* **471**, 177–182 (2011).
4. Sotelo, C. Viewing the brain through the master hand of Ramon y Cajal. *Nat. Rev. Neurosci.* **4**, 71–77 (2003).
5. Mishchenko, Y. *et al.* Ultrastructural analysis of hippocampal neuropil from the connectomics perspective. *Neuron* **67**, 1009–1020 (2010).
6. Denk, W. & Horstmann, H. Serial block-face scanning electron microscopy to reconstruct three-dimensional tissue nanostructure. *PLoS Biol.* **2**, e329 (2004).
7. Knott, G., Marchman, H., Wall, D. & Lich, B. Serial section scanning electron microscopy of adult brain tissue using focused ion beam milling. *J. Neurosci.* **28**, 2959–2964 (2008).
8. Micheva, K.D. & Smith, S.J. Array tomography: a new tool for imaging the molecular architecture and ultrastructure of neural circuits. *Neuron* **55**, 25–36 (2007).
9. Livet, J. *et al.* Transgenic strategies for combinatorial expression of fluorescent proteins in the nervous system. *Nature* **450**, 56–62 (2007).
10. Wickersham, I.R. *et al.* Monosynaptic restriction of transsynaptic tracing from single, genetically targeted neurons. *Neuron* **53**, 639–647 (2007).
11. Feinberg, E.H. *et al.* GFP reconstitution across synaptic partners (GRASP) defines cell contacts and synapses in living nervous systems. *Neuron* **57**, 353–363 (2008).
12. Gordon, M.D. & Scott, K. Motor control in a *Drosophila* taste circuit. *Neuron* **61**, 373–384 (2009).
13. Zhai, R.G. & Bellen, H.J. The architecture of the active zone in the presynaptic nerve terminal. *Physiology* **19**, 262–270 (2004).
14. Fairless, R. *et al.* Polarized targeting of neurexins to synapses is regulated by their C-terminal sequences. *J. Neurosci.* **28**, 12969–12981 (2008).
15. Dean, C. & Dresbach, T. Neuroligins and neurexins: linking cell adhesion, synapse formation and cognitive function. *Trends Neurosci.* **29**, 21–29 (2006).
16. Zhang, C. *et al.* Neurexins physically and functionally interact with GABA(A) receptors. *Neuron* **66**, 403–416 (2010).
17. Tang, W. *et al.* Faithful expression of multiple proteins via 2A-peptide self-processing: a versatile and reliable method for manipulating brain circuits. *J. Neurosci.* **29**, 8621–8629 (2009).
18. Navarro-Quiroga, I., Chittajallu, R., Gallo, V. & Haydar, T.F. Long-term, selective gene expression in developing and adult hippocampal pyramidal neurons using focal in utero electroporation. *J. Neurosci.* **27**, 5007–5011 (2007).
19. Shimshek, D.R. *et al.* Codon-improved Cre recombinase (iCre) expression in the mouse. *Genesis* **32**, 19–26 (2002).
20. Liao, G.Y. & Xu, B. Cre recombinase-mediated gene deletion in layer 4 of murine sensory cortical areas. *Genesis* **46**, 289–293 (2008).
21. Lacaille, J.C., Mueller, A.L., Kunkel, D.D. & Schwartzkroin, P.A. Local circuit interactions between oriens/alveus interneurons and CA1 pyramidal cells in hippocampal slices: electrophysiology and morphology. *J. Neurosci.* **7**, 1979–1993 (1987).
22. Klausberger, T. & Somogyi, P. Neuronal diversity and temporal dynamics: the unity of hippocampal circuit operations. *Science* **321**, 53–57 (2008).
23. Megías, M., Emri, Z., Freund, T.F. & Gulyás, A.I. Total number and distribution of inhibitory and excitatory synapses on hippocampal CA1 pyramidal cells. *Neuroscience* **102**, 527–540 (2001).
24. Belmonte, M.K. *et al.* Autism and abnormal development of brain connectivity. *J. Neurosci.* **24**, 9228–9231 (2004).
25. Petreanu, L., Huber, D., Sobczyk, A. & Svoboda, K. Channelrhodopsin-2-assisted circuit mapping of long-range callosal projections. *Nat. Neurosci.* **10**, 663–668 (2007).
26. Wang, H. *et al.* High-speed mapping of synaptic connectivity using photostimulation in Channelrhodopsin-2 transgenic mice. *Proc. Natl. Acad. Sci. USA* **104**, 8143–8148 (2007).
27. Briggman, K.L., Helmstaedter, M. & Denk, W. Wiring specificity in the direction-selectivity circuit of the retina. *Nature* **471**, 183–188 (2011).
28. Micheva, K.D., Busse, B., Weiler, N.C., O'Rourke, N. & Smith, S.J. Single-synapse analysis of a diverse synapse population: proteomic imaging methods and markers. *Neuron* **68**, 639–653 (2010).

ONLINE METHODS

Constructs and viral production. The chimeric pre- and post-synaptic mGRASP were designed and synthesized from published sequences (NCBI), using codon optimization for *M. musculus* (DNA2.0). Full-length coding sequences for the pre- and post-mGRASP components are available in **Supplementary Note 3**. Signal peptides and transmembrane domains were predicted by bioinformatics servers SignalP[29] (http://www.cbs.dtu.dk/services/SignalP/) and DAS transmembrane prediction server[30] (http://www.sbc.su.se/~miklos/DAS/). Molecular lengths of extracellular domains were simulated using Protein Data Bank[31] and PyMol.

The constructs described in the text were cloned into recombinant aavCAG vector with the *CAG* promoter (CMV enhancer, β-actin promoter and regulatory element from the woodchuck hepatitis virus (*WPRE*)) via BamHI and HindIII digestion. Recombinant adeno-associated viruses (rAAV) were produced and purified by CsCl gradients as described previously[32]. Serotype 1 was used for general infection, while serotype 7 for interneuron infection.

Cre recombinase–dependent 'on' and 'off' mGRASP. To make Cre-dependent mGRASP, at first, the faithful flexed AAV vector (aavCAG-Jx) was generated using *lox66* and *lox71* sites[33]. Two complementary oligos containing *lox66*, HindIII, EcoRV, BglII sites and *lox71* (JK-lox66/71, 5′-gatcATAACTTCGTATAGCATACATTATACGAACGGTAaagcttgatatcagatctATAACTTCGTATAATGTATGCTATACGAACGGTAc-3′ and JK-lox66/71, 5′-agctgTACCGTTCGTATAGCATACATTATACGAAGTTATagatctgatatcaagcttTACCGTTCGTATAATGTATGCTATACGAAGTTAT-3′) were synthesized, annealed and inserted into aavCAG digested by BamHI and HindIII. For the switch 'on' version (aavCAG-Jx-rev-mGRASP), the pre- and post-mGRASP digested by BamHI and HindIII were cloned into the aavCAG-Jx digested by BglII and HindIII. For the switch 'off' version (aavCAG-Jx-mGRASP), the pre- and post-mGRASP constructs digested by Blunted and HindIII were cloned into the paavCAG-Jx digested by EcoRV and HindIII. The iCre-encoding sequence, amplified by PCR[19], was cloned into the aavCAG via BamHI and HindIII.

Gene delivery: *in utero* electroporation and stereotaxic virus injection. All animal procedures were conducted in accordance with protocols approved by the Institutional Animal Care and Use Committee (IACUC) at the Janelia Farm Research Campus, Howard Hughes Medical Institute. Randomization procedures were used for the animals. DNAs (2 μg μl^{-1}) were injected into the right lateral ventricle of embryos from embryonic day 15.5 timed-pregnant C57BL/6J (Charles River). DNAs (paavCAG-iCre or paavCAG-post-mGRASP-2A-dTomato) were purified using EndoFree Plasmid kit (Quiagen) and dissolved in water. Hippocampal CA1 progenitor cells were transfected via *in utero* electroporation[18]. Electroporation was achieved with five pulses (duration 50 ms, frequency 1 Hz, 43.5 V). Adult mice 2–3 months post-electroporation were deeply anesthetized using an isoflurane–oxygen mixture (1% vol isoflurane per vol O_2) and rAAV was injected via stereotaxic surgery[34]. Stereotaxic coordinates of CA1 were anteroposterior (AP) −2.0 mm relative to bregma, mediolateral (ML) +1.6 mm and ventral (V) 1.05–1.15 mm and those of CA3 were AP −2.06 mm, ML −2.4 and −2.625 mm, and V 1.95–2.15 mm ventral. We injected 40–50 nl of viral suspension (titer, ~2×10^{12} pfu ml^{-1} measured by QuickTiter AAV Quantitation Kit, Cell Biolabs) over 1 min using a pulled glass micropipette (tip diameter, 10–20 μm; Drummond). To prevent backflow, the micropipette was left in the brain for over 7 min before it was pulled up.

Brain-slice preparation and immunostaining for light microscopy and electron microscopy. Mice infected with rAAVs were 2–3 weeks later perfused with PBS and 4% paraformaldehyde (PFA) in 0.1 M phosphate buffer (PB, pH 7.4) and post-fixed in 4% PFA for 2 h. For mGRASP imaging, brain slices were sectioned to 100–200 μm thickness with a vibratome (VT1200S, Leica) and were then mounted in ProLong Gold antifade reagent (Invitrogen). For fluorescence immunostaining in LM, 50-μm brain slices were blocked in 0.1% Triton X-100 and 10% goat serum in TBS for 1 h at room temperature (25 °C) and incubated with anti-GFP (1:1,000, Invitrogen and 1:800, Abcam) in 0.05% Triton X-100 and 5% goat serum in TBS overnight 4 °C followed by Alexa Fluor 488–conjugated secondary antibody for 2 h at room temperature. For immuno-silver-gold staining in EM[35], 50-μm brain slices were incubated with anti-GFP (1:1,000, Invitrogen (A11122) and 1:800, Abcam (ab290) in PBS after 10% goat serum blocking overnight 4 °C followed by 3,3′ diamino benzidine tetrahydrochloride (DAB) detection using Vectastain ABC kit according to the manufacturer's protocol (Vector Laboratories). DAB reaction product was silver-gold enhanced by incubating in 2.6% hexamethylenetetramine, 0.2% silver nitrate and 0.2% sodium borate for 10 min at 60 °C followed by 0.05% gold chloride for 2 min and 3% sodium thiosulfate for 2 min. Invitrogen anti-GFP was used for mCerulean (pre-mGRASP) and reconstituted mGRASP, whereas Abcam anti-GFP was used for post-mGRASP.

Image acquisition and data analysis. We acquired images with LSM 710, 510 confocal microscopes (Zeiss) equipped with a mortised stage, and a Macro Zoom System Microscope MVX10 (Olympus). The 8-bit tiled images of the hippocampi of brain sections were obtained at 0.4–0.5 μm depth intervals using ×63 1.4 numerical aperture (NA), ×40 1.3 NA Plan Apochromat oil objectives with 2–4-fold digital zoom controlled by Zeiss software (ZEN 2009) through a motorized stage. To avoid overlapping of signals, three fluorophores (mCerulean, mGRASP and dTomato) were excited with 405-nm, 488-nm and 543-nm wavelength and were imaged in emission wavelengths 441–485 nm, 486–554 nm and 559–639 nm, respectively, using sequential line scanning. Instrument parameter settings were optimized to avoid photobleaching and image saturation. Adjacent stacks had 5–10% overlap to stitch tiled stacks together with precision and trace neurons.

Stitching and computer-aided tracing. The tiles were stitched together to form a single image of the imaging field. Normalized cross-correlation (NCC) was used to determine the relative positions of the tiles. Given two tiles, $T_1(x,y,z)$ and $T_2(x,y,z)$, the NCC method calculates the correlation coefficient for every possible 3D displacement Δ between them. The formula of the calculation can be written as

$$r(\Delta) = \int_{v \in O_\Delta} \left(\frac{[T_1(p) - \mu(T_1(O_\Delta))][T_2(p) - \mu(T_2(O_\Delta))]}{\sigma(T_1(O_\Delta))\sigma(T_2(O_\Delta))} \right) dp$$

where O_Δ is the overlap region between T_1 and T_2 when displaced by the 3D vector with respect to each other, $T_\alpha(O_\Delta)$ is the set of

values of the voxels in T_α over the region O_Δ, and $\mu(A)$ and $\sigma(A)$ are the mean and s.d. of the values in A. Ideally, the desired relative displacement between T_1 and T_2 is the displacement

$$\Delta_0 = \text{argmax}_\Delta r(\Delta)$$

that maximizes the normalized cross-correlation between them. However, for very small overlaps there can be sufficient noise or accidental correlation that they must be eliminated from consideration. Therefore, we simply ignored the NCC values for which O_Δ is smaller than 10^{-6} voxels, which is a safe threshold because the stacks are imaged to overlap by much more than this.

Our tracing algorithm was based on step-wise cylinder fitting. More details about the tracing algorithm can be found in ref. 36. One critical part of the algorithm is to measure how well a cylinder fits to the signal. We used a cylindrical filter that in cross section is the Laplacian of a Gaussian as a neurite fiber in cross section looks like a Gaussian-diffused spot. We start with $U(x,y,z)$, a 'unit cylinder' that has the form

$$U(x,y,z) = (1-(x^2+y^2))e^{-(x^2+y^2)}$$

in which $z \in (-h/2, h/2)$ and then consider the space of all cylindrical filters that can be obtained by taking U and first scaling it symmetrically in x and y by radius r, then rotating it in three dimensions in any manner desired, and at the last, scaling it along the z axis by a factor α that reflects the anisotropy of the point spread function (PSF) of a typical microscope. In our implementation, the length of the cylinder, h, is set to 10 pixels.

When a point is selected on the image by a mouse click, the image signal around the point is examined to determine the position of the seed cylinder. Specifically, the initial cylinder is located at the clicked point with its radius r set to 3 pixels and with its axis parallel to the z axis. To move the cylinder closer toward the medial axis of the target branch, it is shifted to the centroid of local signal. After that, the orientation and size of the cylinder are determined by two steps: coarse search and fine tuning. In the first step, coarse search, we discretized the parameter space, checking each sample point to search for the model that gives the highest score when convolved with the signal. In the second step, fine tuning, the retrieved cylinder was further refined by scaling and rotating as above with a gradient descent procedure. Once the first cylinder is set, it is duplicated and the duplicate is advanced along the cylinder's central axis by 5 pixels in our implementation, where upon it is once again rotated and scaled with a gradient descent procedure to find the best fit to the signal. This walk continues in steps of 5 pixels, as long as the resulting cylinder has a fitting score above a certain threshold.

mGRASP puncta detection. The working area is defined by expanding the radius of each reconstructed neurite cylinder with the interval by the length of typical spines (on average 2–2.5 μm). To handle brightness variation in puncta, the detection was conducted sequentially from the gray level of the brightest puncta to the gray level just above background. The final result is the union of the puncta extracted from all the gray levels. For detecting puncta at each gray level, there are three major steps. Note that the parameter values in these steps described below were mainly determined empirically based on the criterion that both false positive and negative detection rates should be low.

The first step is a rough estimation of puncta locations at a given gray level. The only pixels considered for matching are those (i) greater than the current gray level and (ii) not part of a match to a puncta at a greater gray level. This is accomplished by setting all pixels other than those just described to 0 in a 'masked' copy of image volume. Then NCC between the masked image and a Gaussian kernel is calculated where this kernel is as follows

$$G(x,y,z) = \frac{1}{\sqrt{2\pi\sigma_{xy}\sigma_z}} e^{-\left(\frac{x^2+y^2}{2\sigma_{xy}^2}+\frac{z^2}{2\sigma_z^2}\right)}$$

where $\sigma_{xy} = 0.25$ μm and $\sigma_x = 0.5$ μm.

This defines a ball with radius 0.25 μm in physical space that matches the minimal size of a punctum. We determined this radius value by visually checking a population of puncta in our data. Any location whose NCC convolution with the kernel was above the mean and locally maximal was taken as an initial estimate of a puncta location.

The second step refines locations of the puncta and estimates their sizes. This is done through an iterative mean-shift procedure. In this procedure, given a punctum with estimated location p and radius r, a potentially better estimation of the real punctum location is the centroid c of all pixels inside the ball with center p and radius $1.1r$. If this gives a better NCC score than the 'shift' is accepted and iterated upon, otherwise the current configuration is taken as the final estimate of the punctum.

The final step is to merge puncta estimates that actually cover one large punctum. To determine whether two puncta should be merged, the distance between their centers is checked first. If the distance is less than 2 μm, then the intensity profile of any line segment connecting the two centers was examined. The two puncta would be merged if the valley of this line profile was lower than the smallest foreground value. After merging, the center and radius of the new punctum was re-estimated by the same mean-shift procedure, in which the initial center was set to the average of the two original centers and the initial radius was set to the sum of the two original radii.

Reconstructed neurons and detected mGRASP puncta are visualized in Vaa3D[37] (http://vaa3d.org/).

29. Petersen, T.N., Brunak, S., von Heine, G. & Nielsen, H. SignalP 4.0: discriminating signal peptides from transmembrane regions. *Nat. Methods* **8**, 785–786 (2011).
30. Cserzo, M., Wallin, E., Simon, I., von Heijne, G. & Elofsson, A. Prediction of transmembrane alpha-helices in procaryotic membrane proteins: the Dense Alignment Surface method. *Protein Eng.* **10**, 673–676 (1997).
31. Berman, H.M. *et al.* The Protein Data Bank. *Nucleic Acids Res.* **28**, 235–242 (2000).
32. Grieger, J.C., Choi, V.W. & Samulski, R.J. Production and characterization of adeno-associated viral vectors. *Nat. Protoc.* **1**, 1412–1428 (2006).
33. Zhang, Z. & Lutz, B. Cre recombinase-mediated inversion using lox66 and lox71: method to introduce conditional point mutations into the CREB-binding protein. *Nucleic Acids Res.* **30**, e90 (2002).
34. Komai, S., Seeburg, P.H. & Osten, P. Stereotaxic gene delivery in the rodent brain. *Nat. Protoc.* **1**, 3166–3173 (2006).
35. Petralia, R.S. *et al.* Organization of NMDA receptors at extrasynaptic locations. *Neuroscience* **167**, 68–87 (2010).
36. Zhao, T. *et al.* Automated reconstruction of neuronal morphology based on local geometrical and global structural models. *Neuroinformatics* **9**, 247–261 (2011).
37. Peng, H., Ruan, Z., Long, F., Simpson, J.H. & Myers, E.W. V3D enables real-time 3D visualization and quantitative analysis of large-scale biological image data sets. *Nat. Biotechnol.* **28**, 348–353 (2010).

doi:10.1038/nmeth.1784